Design of Dual-Magnet Memory Machines

Fuhua Li, K.T. Chau, and Chunhua Liu
Dept. of Electrical and Electronic Engineering, University of Hong Kong, Hong Kong, China
E-mail: fhli@eee.hku.hk

Abstract — The memory machine, which adopts the aluminum-nickel-cobalt (AlNiCo) as the permanent magnet (PM) material, has attracted a wide attention. In this paper, by incorporating two kinds of PM materials including the neodymium-iron-boron (NdFeB) and the AlNiCo, the dual-magnet memory machine is proposed, which has more distinguished merits than its single-magnet counterpart. Due to the high coercivity of the NdFeB, the overall power density is augmented notably. Also, the risk of accidental demagnetization is significantly reduced. Most importantly, the design on how to combine these two kinds of PMs is discussed in detail, with emphasis on their shape, thickness and relative position. Both simulation and experimentation are given to illustrate the validity of the proposed design.

I. INTRODUCTION

With more concerns about environmental protection and global warming, electric vehicles (EVs) have been gaining more and more attention. Due to the limitation of their battery energy storage, there is a pressing need on the development of energy-efficient machines [1-9]. Compared with conventional permanent magnet (PM) brushless machines, the memory machine [10-17] takes the advantage of tunable air-gap flux while retaining high efficiency and high power density. Moreover, compared with latest PM hybrid machines [18-23], the memory machine is not required to continually excite the DC field windings, hence improving the operating efficiency.

The memory machine does have some drawbacks. Firstly, the aluminum-nickel-cobalt (AlNiCo) PM has a relatively lower energy product than the neodymium-iron-boron (NdFeB) PM, thus degrading the overall power density. Secondly, the AlNiCo has a low coercivity which increases the possibility of accidental demagnetization. Thirdly, the demagnetization characteristic of the AlNiCo PM is very nonlinear which inevitably involves the hysteresis effect when performing electromagnetic field analysis. However, the distinguished merits and special performances of memory machines are still quite attractive for practical applications.

The purpose of this paper is to propose a dual-magnet topology for the memory machine, the so-called dual-magnet memory machine. The key is to use the NdFeB PM to complement with the AlNiCo PM in such a way that the overall power density can be maintained while offering the definite merit of online tunable flux. Additionally, by adopting an outer-rotor doubly salient stator-PM structure [24-36], the machine offers the advantages of high robustness of the rotor and full utilization of the inner space of the stator. These merits are highly desirable by in-wheel motors for EVs.

Additionally, The shape, thickness and relative position of the two kinds of PMs are so optimized that the range of air-gap flux control can be maximized while the overall power density can be maintained. And the time step finite element method (TS-FEM) [37] [38] is used to analyze the proposed machine under various dual-magnet arrangements. Then, the optimal design is prototyped and tested to verify the validity of the proposed machine design.

II. DESIGN

Fig. 1 shows the structure of the proposed dual-magnet memory machine. It adopts 5 phases, rather than the conventional 3 phases, aiming to offer smoother output torque which is desirable for direct-drive EV application. The out-rotor includes 24 salient poles and the stator consists of 30 salient poles. The dual-magnet arrangement is located within each dashed box.

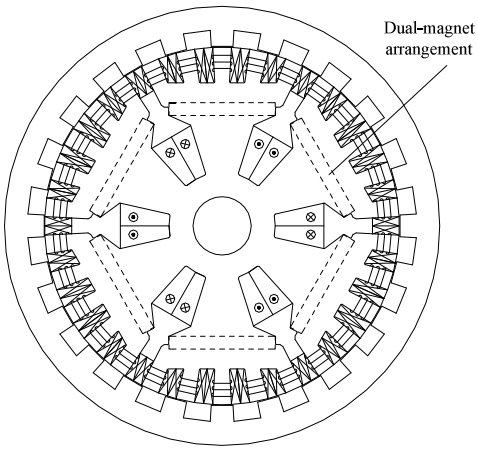

Fig. 1. Structure of dual-magnet memory machine.

Three types of arrangements are shown in Fig. 2. The magnets in Fig. 2 (a) and (b) are placed closed together to obtain the maximum integrated magnetic field. The top aligned arrangement is often used in surface mount PM machines to have unified surface. The center aligned arrangement has more balanced flux distribution. But in Fig. 2 (c) the iron bridges between them can be tuned to amplify the flux weakening capability. These types are all analyzed in later content by TS-FEM simulation under the same motor structure.

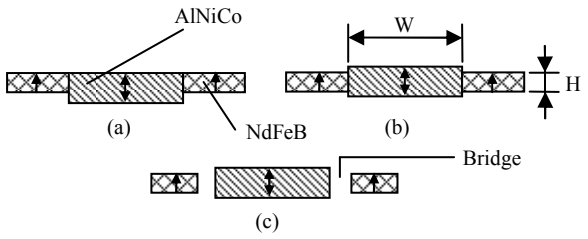

Fig. 2. Dual-magnet arrangements. (a) Top aligned without bridges. (b) Center aligned without bridges. (c) Center aligned with bridges.

Typically, the thickness of magnets is determined by rated

power. The thicker the magnets, the stronger the ability is to resist demagnetization. The AlNiCo PMs should be thicker than the NdFeB PMs because of the low coercivity of AlNiCo. The thickness of AlNiCo PMs is determined by the needed magnetomotive force (MMF), rated current of magnetizing windings and slot fill factor. The $3H_c$ MMF can be calculated by (1):

$$F = 3F_{AlNiCo} + F_{airgap} = 3H_c 2H + \frac{B_\delta}{\mu_0} 2\delta \qquad (1)$$

where,

H_c - The coercivity of AlNiCo.

H - The thickness of AlNiCo magnet.

B_δ - The flux density of air-gap.

μ_0 - The permeability of free space.

δ - The thickness of air-gap.

The coefficient 3 in (1) means it takes at least 3 times coercive force to fully magnetize the AlNiCo PMs. The coefficient 2 indicates there are two PMs and two air-gaps in a magnetic loop.

In this design, the rated power is 1500W; the NdFeB PMs are selected to be 4mm thick; each magnetizing winding has 200 turns. Three different models of AlNiCo PMs corresponding to three arrangements in Fig. 2 are simulated by TS-FEM as shown in Fig. 3-Fig. 5. All three models work in generating mode under no load 600rpm.

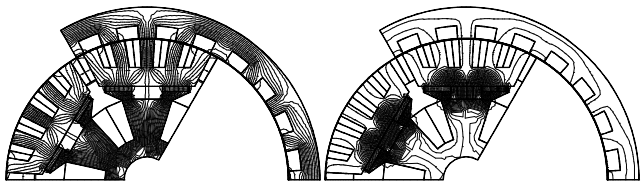

(a) (b)

Fig. 3. Flux distribution of model-1. W_{AlNiCo} =24mm, H_{AlNiCo} =10mm, W_{NdFeB} = 20.4mm, H_{NdFeB} = 4 mm, (a) Magnetizing Current I_M = 20A. (b) I_M = -10A.

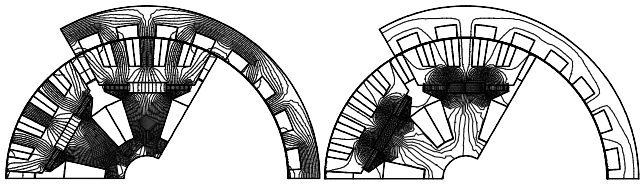

(a) (b)

Fig. 4. Flux distribution of model-2. W_{AlNiCo} = 30mm, H_{AlNiCo} = 8mm, W_{NdFeB} = 17.4mm, H_{NdFeB} = 4 mm, (a) I_M = 10A. (b) I_M = -10A.

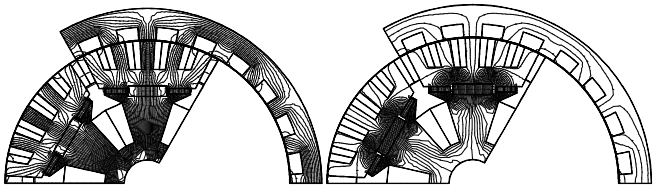

(a) (b)

Fig. 5. Flux distribution of model-3. W_{AlNiCo} = 30mm, H_{AlNiCo} = 8mm, W_{NdFeB} = 15.4mm, H_{NdFeB} = 4 mm, (a) I_M =10A. (b) I_M = -10A.

In Fig. 3, the thickness of top-aligned AlNiCo PMs is 10mm. After using 20A current to magnetize the AlNiCo PMs, the AlNiCo PMs have the same magnetic polar direction as the neighboring NdFeB PMs. On one hand, it can be seen there are few flux lines though the magnets shown in Fig. 3 (a). That means the AlNiCo PMs contribute little to transfer the energy to the air-gap, resulting in low power density. An important reason is that the width of one AlNiCo PM is too narrow comparing with the sum of the width of two neighboring NdFeB PMs and hence NdFeB PMs have significant effect on AlNiCo PMs. On the other hand, flux lines in top-aligned arrangement are not evenly distributed in corners of AlNiCo PMs, owing to the relative position with NdFeB PMs. Although it can realize flux weakening when AlNiCo PMs are reversely magnetized, shown in Fig. 3 (b), meaning that the AlNiCo PMs have reverse magnetic polar direction with the neighboring NdFeB PMs, the overall performance of model-1 is not preferred. Therefore, the center-aligned arrangement is adopted to achieve a more balanced flux distribution.

As shown in Fig. 4 (a) and (b), flux lines pass evenly through the whole AlNiCo PMs in center-aligned model in the cases of 10A current magnetizing and -10A current reversely magnetizing. It shows the thickness and width of the two kinds of PMs are better matched.

In Fig. 5 (a), the model-3 with 2mm bridges has more concentrated flux lines through the middle part of AlNiCo PMs comparing with model-1 and model-2. It indicates that the effect of NdFeB PMs is reduced and AlNiCo PMs play a greater role in energy delivery. Fig. 5 (b) shows few flux lines pass through bridges during the reverse magnetization.

Fig. 6 shows the cogging torques of these models without skewing under 10A current magnetization. It can be seen that they have similar waveforms but different amplitudes owing to the same salient pole structure but different PM dimension.

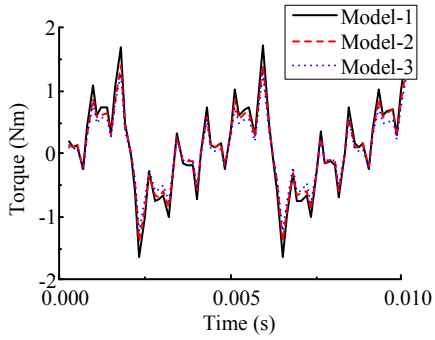

Fig. 6. Cogging torques of three models

III. Effect of Bridge

Since the interaction between AlNiCo PMs and NdFeB PMs is significantly intensive in adjacent sides, some flux lines of AlNiCo PMs near the interface are looped through NdFeB PMs. Inspired by this feature, if a bridge is added between an AlNiCo PM and a NdFeB PM, forming a narrow additional path to let the NdFeB PM release flux, it will reduce the effect on AlNiCo PMs. With this bridge, when AlNiCo PMs have the same polarity with neighboring NdFeB PMs, more flux lines will pass through AlNiCo PMs, which means more energy will be delivered by AlNiCo PMs. When AlNiCo PMs have reverse polarity with neighboring NdFeB PMs, the bridges will help to weakening the air-gap flux density. Generally by this means, the memory machine has

more capacity to realize the memory function, in other words, the flux weakening ability is augmented.

The model-3 with bridges of different widths, whose structure is in accordance with Fig. 5, is simulated in the condition of 200V DC drive voltage and 5A armature current. By using TS-FEM, the performances of different bridges are calculated and analyzed, including the magnetic field distribution, air-gap flux distribution and staring performance.

First, the dynamic magnetic field distribution is analyzed and shown in Fig. 7-Fig. 10. The relative positions of the rotor and stator are corresponding to the end time of simulation. Different positions are resulted by their own staring processes.

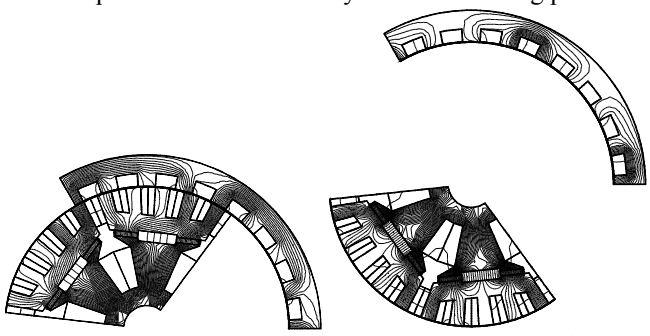

(a) I_M =15A, 15Nm load. (b) I_M = -5A, 5Nm load

Fig. 7. Flux distribution when Bridge = 0mm

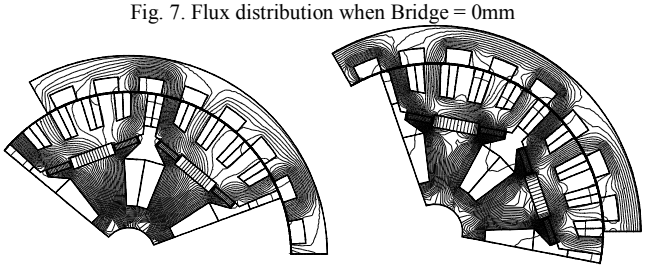

(a) I_M =15A, 15Nm load. (b) I_M = -5A, 5Nm load

Fig. 8. Flux distribution when Bridge =1.2mm

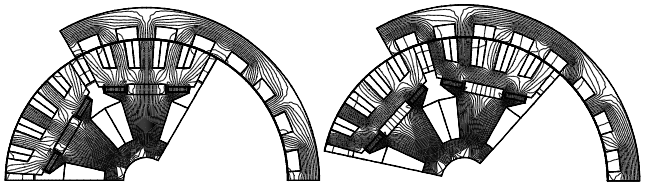

(a) I_M =15A, 15Nm load. (b) I_M = -5A, 5Nm load

Fig. 9. Flux distribution when Bridge = 2.0mm

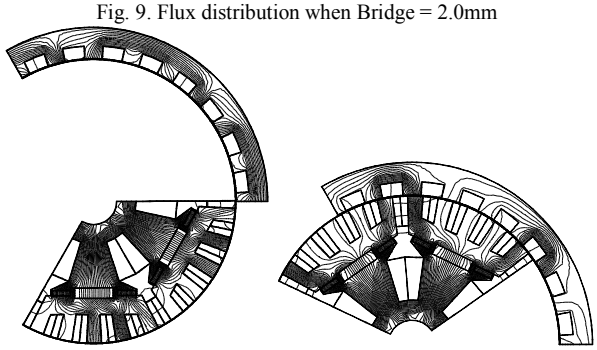

(a) I_M =15A, 15Nm load. (b) I_M = -5A, 5Nm load

Fig. 10. Flux distribution when Bridge = 3.6mm

Assuming that the state of AlNiCo PMs is in the origin of coordinates of BH plane, when the magnetizing current is positive, AlNiCo PMs have the same polar direction as neighboring NdFeB PMs. It can be seen that with bridge width increased from 0 to 3.6mm; more flux lines pass through AlNiCo PMs and also more flux lines passing through the bridges. With the effect of NdFeB reduced by bridges, AlNiCo PMs play a greater role in energy delivery. It should be noted that the flux in bridges does not take part in useful energy delivery, which will reduce the rated load torque. So it is expected that the bridge be as narrow as possible while meeting the torque requirement.

Second, the air-gap flux density, corresponding to the simulation end time, is shown in Fig. 11. It indicates the energy delivering capacity and also the power density of the models. In the Fig. 11 (a), (c) and (e), the average values of positive air-gap flux density are similar, which in accordance with similar steady-state speed as described in later content. The model with 1.2mm bridges has the highest air-gap flux density amplitude exceeding 1.0T. In these two conditions, the 3.6mm bridge model has the lowest air-gap flux density, which means the lowest load capacity.

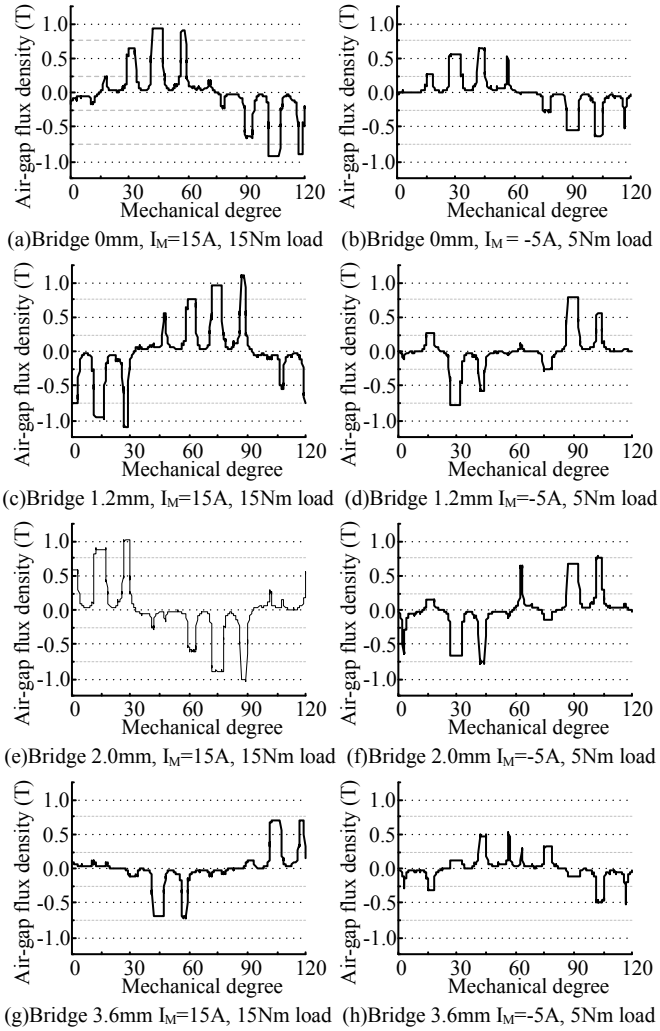

(a)Bridge 0mm, I_M=15A, 15Nm load (b)Bridge 0mm, I_M = -5A, 5Nm load

(c)Bridge 1.2mm, I_M=15A, 15Nm load (d)Bridge 1.2mm I_M=-5A, 5Nm load

(e)Bridge 2.0mm, I_M=15A, 15Nm load (f)Bridge 2.0mm I_M=-5A, 5Nm load

(g)Bridge 3.6mm I_M=15A, 15Nm load (h)Bridge 3.6mm I_M=-5A, 5Nm load

Fig. 11. Air-gap flux density under different bridge width

Third, the dynamic starting torque is presented in Fig. 12. The model with 1.2mm bridges has the highest staring torque shown in figure 12 (c). The starting torque of the model without bridges is lower than 1.2mm and 2.0mm bridge models by nearly 75 percent under 15A magnetization current

and 15Nm load, so it has lower acceleration speed. For the reverse magnetizing, shown in Fig. 12 (b), (d), (f), because the flux of all models are reduced, it takes a short period about 0.12s to change the direction of flux lines, resulting in a short lasting negative torque, during which the models are standing still. The last model with 3.6mm bridges has poor performance comparing with other models, shown in Fig. 15 (g), (h), although it can generate a certain amount of torque to start, it quickly slows down to creep.

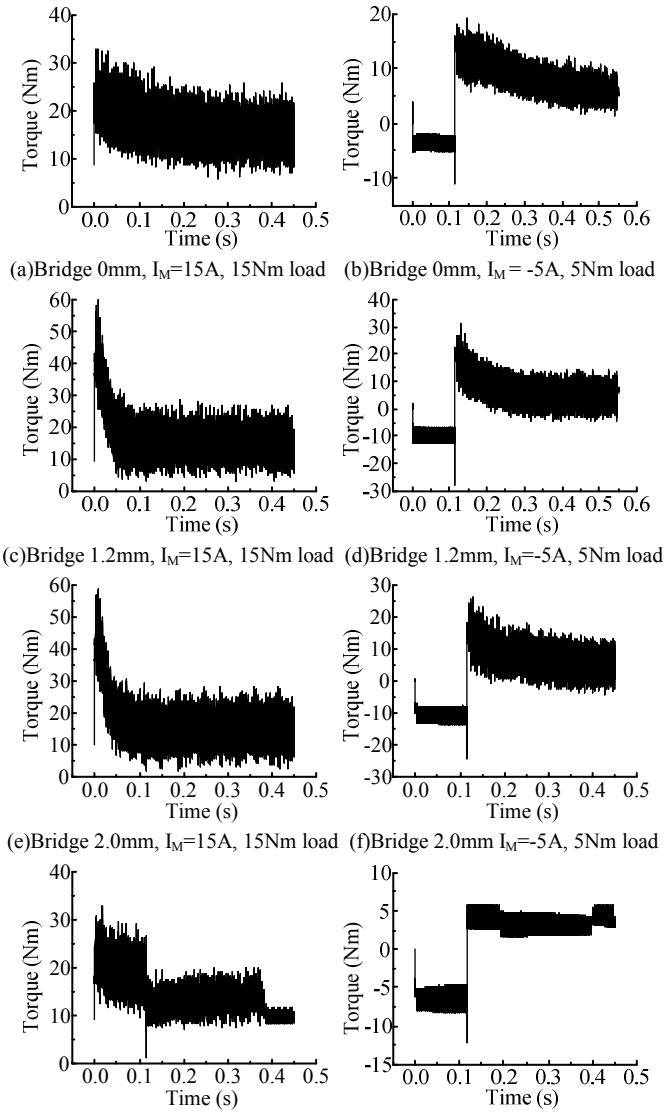

(a)Bridge 0mm, I_M=15A, 15Nm load (b)Bridge 0mm, I_M = -5A, 5Nm load

(c)Bridge 1.2mm, I_M=15A, 15Nm load (d)Bridge 1.2mm, I_M=-5A, 5Nm load

(e)Bridge 2.0mm, I_M=15A, 15Nm load (f)Bridge 2.0mm I_M=-5A, 5Nm load

(g)Bridge 3.6mm I_M=15A, 15Nm load (h)Bridge 3.6mm I_M=-5A, 5Nm load

Fig. 12. Staring torque under different bridge width

Finally, the dynamic starting processes are also simulated by applying different magnetizing current. The acceleration curves under different bridge width are shown in Fig. 13-Fig. 15. When the magnetizing current is 15A, in Fig. 13, the models with bridge width 1.2mm and 2.0mm have larger acceleration speed due to the weakened flux, but have the same steady-state speed with the one without bridges. This means when the AlNiCo PMs are fully magnetized, narrow bridges affect little the load capacity but increase the response speed. But if the bridge is broad like 3.6mm, the load capacity dropped significantly and the model cannot work under 15Nm load.

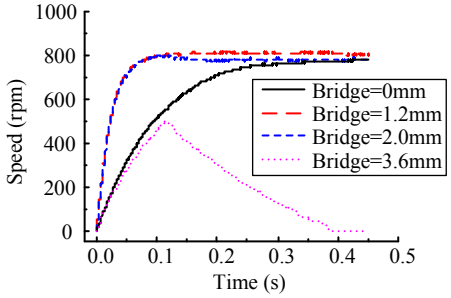

Fig. 13. Acceleration curve under 15Nm load I_M=15A

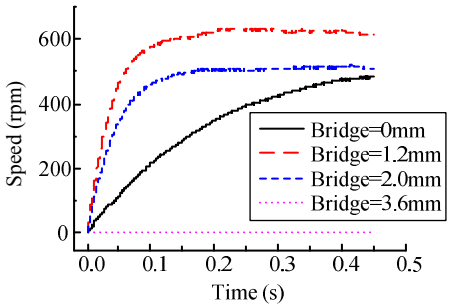

Fig. 14. Acceleration curve under 15Nm load I_M=5A

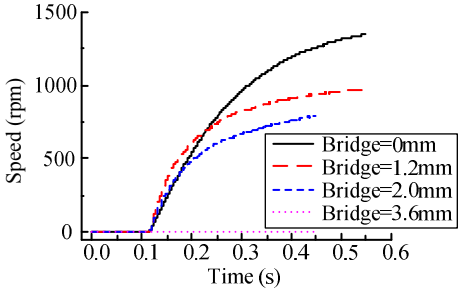

Fig. 15. Acceleration Curve under 5Nm load I_M=-5A

Fig. 14 presents the case under 5A magnetizing current. The models decline in steady state speed, but the 1.2mm model keeps higher. This demonstrates the merit of the bridge. While the AlNiCo PMs are weak magnetized, narrow bridges reduce the effect of NdFeB PMs and further retain higher speed simultaneously providing enough torque. Fig. 15 shows the reversely magnetization case. When AlNiCo PMs have reverse polarity with neighboring NdFeB PMs, most flux lines are inner looped not passing through rotor and the load capacity drops. The model without bridges can maintain higher flux density. It has higher speed than others under light load.

As shown above, the width of bridge plays an important role in the motor performance. Therefore, appropriate width could enhance the motor flux weakening performance, especially the staring torque. For the motor structure of this design, the best choice of bridge is between 1mm to 1.5mm.

IV. Experiment

The prototype of this dual-magnet memory motor, corresponding to the structure shown in Fig.1 and Fig. 2 (b) and the aforementioned model-2, has been made to verify the design. The PM material adopted AlNiCo 5DG and NdFeB

N35. The test-bed is presented in Fig. 16, which includes the memory motor, a DC motor, a torque sensor, a laser tachometer, an electrical load and a 5-phase full-bridge circuit.

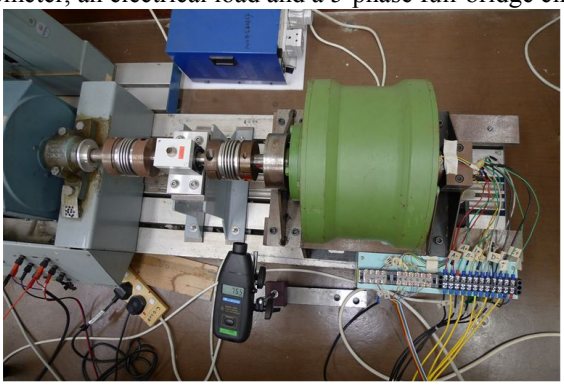

Fig. 16. Dual-magnet memory motor prototype and test-bed

Firstly, the prototype is tested under the generating mode. It is driven by the connected DC motor and working as a generator. According to the calculation, 10A magnetizing current can realize $3H_c$ MMF. After magnetizing the AlNiCo PMs by 10A current, the AlNiCo PMs have the same polarity with the NdFeB PMs and have high remnant magnetism, so the compound magnetic field is intensified to a high level. Then the prototype is driven to 600rpm. The generated back electromotive force (EMF) of one phase is shown in Fig. 17 (a). It can be found the generated EMF has amplitude of 77V. After that, -5A current is used to reversely magnetize the AlNiCo PMs. The tested back EMF has amplitude of 44.4V shown in Fig. 18 (b). In this case, the AlNiCo PMs still have the same polarity with NdFeB PMs, but have lower remanence and hence the back EMF declines. This verifies the memory function and flux weakening ability in the first step.

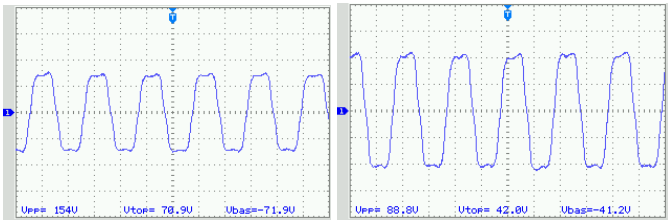

(a) I_M = 10A (b) I_M = -5A

Fig. 17. Motor back EMF under 600rpm

Secondly, the prototype is tested in the no load motor mode. The overall DC drive current is limited to 3A by the control system. The AlNiCo PMs are reversely magnetized by -10A current. Increasing the DC drive voltage from 40V to 220V, the tested no load steady-state speed is shown by the curve with square symbols in Fig. 18. Then, the AlNiCo PMs are magnetized by10A current. The speed under the same DC voltage is shown by the round symbols. As can be seen that the no load performances are approximately similar in the two situations of fully same directional magnetization and fully reverse magnetization. That means the flux weakening operation does not demonstrate its function in the no load case. Additionally, the speed in the same directional magnetization case is a little faster when the voltage greater than 100V. This is because the PMs can provide higher flux density in the case of 10A magnetization.

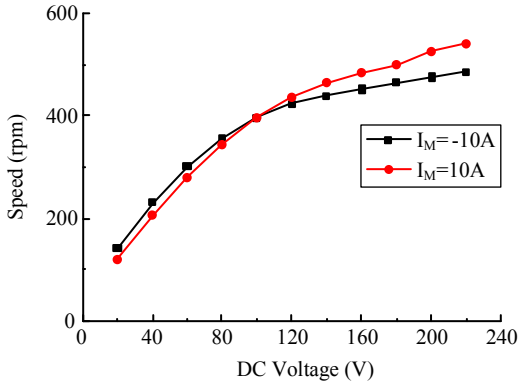

Fig. 18. No load speed vs. DC voltage curve

Thirdly, the test was carried out by using different magnetizing current under the same 5Nm load exerted by the DC motor and the electrical load. The AlNiCo PMs were successively magnetized by 10A, -5A, -10A, 5A current. The corresponding steady-state speeds are shown in Fig. 19. It shows different magnetization levels result in different speeds when the DC drive voltage and load are fixed. That means this memory motor can tune its speed in a certain range to meet different speed requirements in no need to change the drive voltage, while providing the same torque. When operating in 220V voltage with 5Nm load, the speed range achieves 300rpm, 67% of the highest speed.

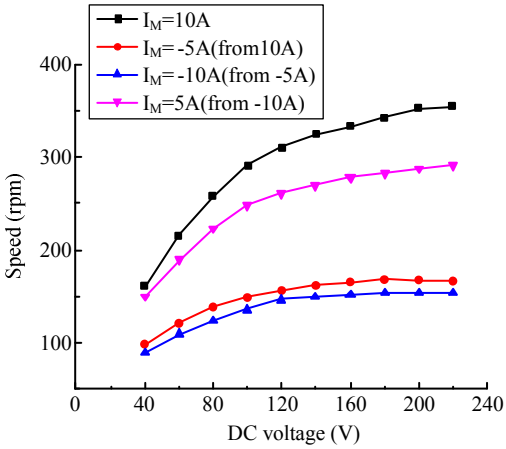

Fig. 20. Speed vs. DC voltage curve with 5Nm load

V. CONCLUSION

A design of memory machines with dual-magnet structure is presented in this paper. First, three types of arrangements are discussed. Subsequently, the effect of iron bridges are analyzed by TS-FEM and simulated in details. The result shows appropriate narrow bridges between AlNiCo PMs and NdFeB PMs promote the flux weakening capacity and hence the starting torque. The bridges enable a fast acceleration during a starting process, which is highly desired in EV applications. Finally, a prototype is made to verify the design. According to the experiment result, the memory motor can have a wide speed range achieved by flux-weakening operation - changing the magnetization level of AlNiCo PMs.

ACKNOWLEDGMENT

This work was supported by a grant (Project No. HKU710710E) from the Hong Kong Research Grants Council, Hong Kong Special Administrative Region, China.

VI. REFERENCES

[1] K.T. Chau and C.C. Chan, "Emerging energy-efficient technologies for hybrid electric vehicles," Proceedings of IEEE, vol. 95, no. 4, April 2007, pp. 821-835.

[2] K.T. Chau, D. Zhang, J.Z. Jiang, C. Liu and Y.J. Zhang, "Design of a magnetic-geared outer-rotor permanent-magnet brushless motor for electric vehicles," IEEE Transactions on Magnetics, vol. 43, no. 6, June 2007, pp. 2504-2506.

[3] K.T. Chau, W. Cui, J.Z. Jiang and Z. Wang, "Design of permanent magnet brushless motors with asymmetric air gap for electric vehicles," Journal of Applied Physics, vol. 99, no. 8, April 2006, paper no. 80R322, pp. 1-3.

[4] C. Liu, K.T. Chau and J.Z. Jiang, "A permanent-magnet hybrid brushless integrated-starter-generator for hybrid electric vehicles," IEEE Transactions on Industrial Electronics, vol. 57, no. 12, December 2010, pp.4055-4064.

[5] Y. Fan and K.T. Chau, "Development of doubly salient permanent magnet motors for electric vehicles," Journal of Asian Electric Vehicles, vol. 3, no. 1, June 2005, pp. 689-695.

[6] K.T. Chau, C.C. Chau, and C. Liu, "Overview of permanent magnet brushless drives for electric and hybrid electric vehicles," IEEE Transactions on Industrial Electronics, Vol. 55, No. 6, pp. 2246-2257, June 2008.

[7] M. Cheng, Y. Fan and K.T. Chau, "Design and analysis of a novel stator-doubly-fed doubly salient motor for electric vehicles," Journal of Applied Physics, vol. 97, no. 10, May 2005, paper no. 10Q508, pp. 1-3.

[8] K.T. Chau, C.C. Chan and C. Liu, "Overview of permanent-magnet brushless drives for electric and hybrid electric vehicles," IEEE Transactions on Industrial Electronics, vol. 55, no. 6, June 2008, pp. 2246-2257.

[9] Y. Fan and K.T. Chau, "Design, modeling, and analysis of a brushless doubly fed doubly salient machine for electric vehicles," IEEE Transactions on Industry Applications, vol. 44, no. 3, May-June 2008, pp. 727-734.

[10] V. Ostovic, "Memory motor-A new class of controllable flux PM machines for a true wide speed operation," in Proc. Conf. Rec. IEEE-IAS Annual Meeting, 2001, pp. 2577–2584.

[11] V. Ostovic, "Pole changing permanent magnet machines," IEEE Trans. Ind. Appl., vol. 38, no. 6, pp. 1493–1499, Dec. 2002.

[12] C. Yu, K.T. Chau and J. Z. Jiang, "A flux-mnemonic permanent magnet brushless machine for wind power generation," Journal of Applied Physics, vol. 105, no. 7, April 2009, paper no. 07F114, pp. 1-3.

[13] C. Yu and K. T. Chau, "Design, Analysis, and Control of DC-Excited Memory Motors," IEEE Transactions on Energy Conversion, vol. 26, no. 2, June 2011, pp. 479-489.

[14] C. Yu, K.T. Chau, X. Liu and J.Z. Jiang, "A flux-mnemonic permanent magnet brushless motor for electric vehicles," Journal of Applied Physics, vol. 103, no. 7, April 2008, paper no. 07F103, pp. 1-3.

[15] X. Zhu, M. Cheng, K.T. Chau and C. Yu, "Torque ripple minimization of flux-controllable stator-permanent-magnet brushless motors using harmonic current injection," Journal of Applied Physics, vol. 105, no. 7, April 2009, paper no. 07F102, pp. 1-3.

[16] J. H. Lee, and J. P. Hong, "Permanent magnet demagnetization characteristic analysis of a variable flux memory motor using coupled Preisach modeling and FEM," IEEE Transactions on Magnetics, vol. 44, no. 6, pp. 1550-1553, June 2008

[17] X. Zhu, K.T. Chau, M. Cheng and C. Yu, "Design and control of a flux-controllable stator-permanent magnet brushless motor drive," Journal of Applied Physics, vol. 103, no. 7, April 2008, paper no. 7F134, pp. 1-3.

[18] C. Liu, K.T. Chau, W. Li and C. Yu, "Efficiency optimization of a permanent-magnet hybrid brushless machine using dc field current control," IEEE Transactions on Magnetics, vol. 45, no. 10, October 2009, pp. 4652-4655.

[19] C. Liu, K.T. Chau, and J.Z. Jiang, "Design of a new outer-rotor permanent-magnet hybrid machine for wind power generation," IEEE Transactions on Magnetics, Vol. 44, No. 6, June 2008,pp. 1494-1497.

[20] C. Liu, K.T. Chau, and X. Zhang, "An efficient wind-photovoltaic hybrid generation system using doubly-excited permanent-magnet brushless machine," IEEE Transactions on Industrial Electronics. Vol. 57, No. 3, March 2010,pp. 831-839,.

[21] C. Liu, K.T. Chau, and W. Li, "Comparison of fault-tolerant operations for permanent-magnet hybrid brushless motor drive," IEEE Transactions on Magnetics, Vol. 46, No. 6, pp. 1378-1381, June 2010.

[22] K.T. Chau, Y.B. Li, J.Z. Jiang and S. Niu, "Design and control of a PM brushless hybrid generator for wind power application," IEEE Transactions on Magnetics, vol. 42, no. 10, October 2006, pp. 3497-3499.

[23] C. Liu, K.T. Chau, and W. Li, "Loss analysis of permanent magnet hybrid brushless machines with and without HTS field windings," IEEE Transactions on Applied Superconductivity, Vol. 20, No. 3, pp. 1077-1080, June 2010.

[24] K.T. Chau, Y.B. Li, J.Z. Jiang and C. Liu, "Design and analysis of a stator-doubly-fed doubly-salient permanent-magnet machine for automotive engines," IEEE Transactions on Magnetics, vol. 42, no. 10, October 2006, pp. 3470-3472.

[25] K.T. Chau, Q. Sun, Y. Fan and M. Cheng, "Torque ripple minimization of doubly salient permanent magnet motors," IEEE Transactions on Energy Conversion, vol. 20, no. 2, June 2005, pp. 352-358.

[26] C. Liu, K.T. Chau, J.Z. Jiang and S. Niu, "Comparison of stator-permanent-magnet brushless machines," IEEE Transactions on Magnetics, vol. 44, no. 11, November 2008, pp. 4405-4408.

[27] J. Gan, K.T. Chau, Y. Wang, C.C. Chan and J.Z. Jiang, "Design and analysis of a new permanent magnet brushless dc machine," IEEE Transactions on Magnetics, vol. 36, no. 5, September 2000, pp. 3353-3356.

[28] L. Jian, K.T. Chau and J.Z. Jiang, "A magnetic-geared outer-rotor permanent-magnet brushless machine for wind power generation," IEEE Transactions on Industry Applications, vol. 45, no. 3, May/June 2009, pp. 954-962.

[29] Y. Fan, K.T. Chau and S. Niu, "Development of a new brushless doubly fed doubly salient machine for wind power generation, IEEE Transactions on Magnetics, vol. 42, no. 10, October 2006, pp. 3455-3457.

[30] Y. Fan and K.T. Chau, "Torque ripple minimization of four-phase doubly salient permanent magnet motors using two-phase operation," Electric Power Components and Systems, vol. 34, no. 4, April 2006, pp. 401-415.

[31] Y. Fan, K.T. Chau and M. Cheng, "A new three-phase doubly salient permanent magnet machine for wind power generation," IEEE Transactions on Industry Applications, vol. 42, no. 1, January/February 2006, pp. 53-60.

[32] K.T. Chau, J.Z Jiang and Y. Wang, "A novel stator doubly fed doubly salient permanent magnet brushless machine," IEEE Transactions on Magnetics, vol. 39, no. 5, September 2003, pp. 3001-3003.

[33] M. Cheng, K.T. Chau, C.C. Chan and Q. Sun, "Control and operation of a new 8/6-pole doubly salient permanent magnet motor drive," IEEE Transactions on Industry Applications, vol. 39, no. 5, September/October 2003, pp. 1363-1371.

[34] M. Cheng, K.T. Chau, and C.C. Chan, "Design and analysis of a new doubly salient permanent magnet motor," IEEE Transactions on Magnetics, vol. 37, no. 4, July 2001, pp. 3012-3020.

[35] Y. Gong, K.T. Chau, J.Z. Jiang, C. Yu and W. Li, "Design of doubly salient permanent magnet motors with minimum torque ripple," IEEE Transactions on Magnetics, vol. 45, no. 10, October 2009, pp. 4704-4707.

[36] C. Liu, K.T. Chau, and W. Li, "Design and Analysis of a HTS Brushless Doubly-fed Doubly-salient Machine," IEEE Transactions on Applied Superconductivity, vol 21, no.3, pp. 1119-1122 June 2011.

[37] Y. Zhang, K.T. Chau, J.Z. Jiang, D. Zhang and C. Liu, "A finite element – analytical method for electromagnetic field analysis of electric machines with free rotation," IEEE Transactions on Magnetics, vol. 42, no. 10, October 2006, pp. 3392-3394.

[38] Y. Gong, K.T. Chau, J.Z. Jiang, C. Yu and W. Li, "Analysis of doubly salient memory motors using Preisach theory," IEEE Transactions on Magnetics, vol. 45, no. 10, October 2009, pp. 4676-4679.